iScience

Article

Single-cell transcriptomics reveals pediatric immune responses to COVID-19 vaccination

Graphical abstract

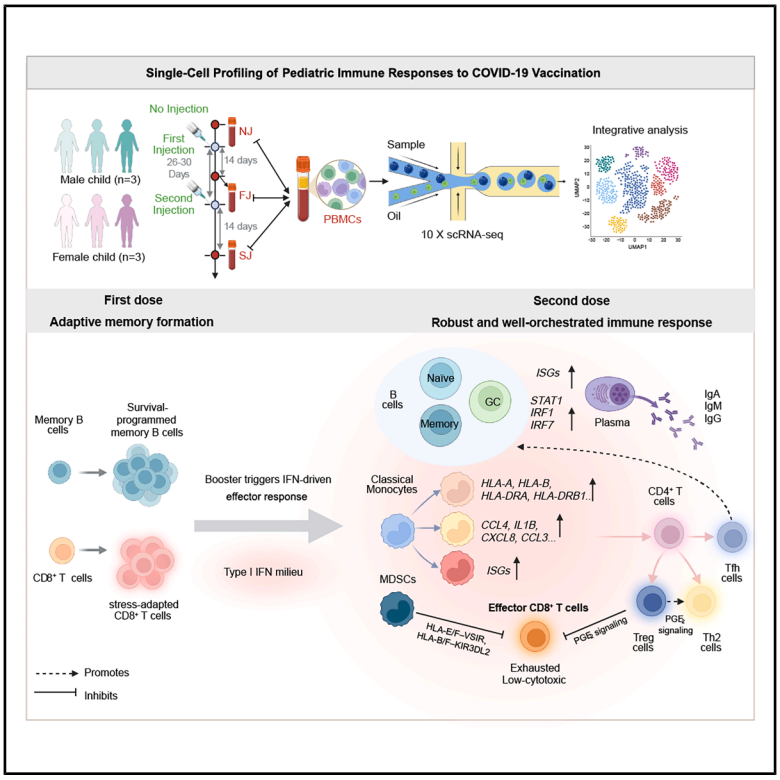

Highlights

- Single-cell transcriptomics delineates pediatric immunity to inactivated COVID-19 vaccine
- Primary dose builds memory B and stress-adapted $CD8^+$ T cells; booster elicits IFN responses
- Monocytes acquire pro-inflammatory, antigen-presenting states with IFN-stimulated genes
- Expanded MDSCs and Tregs restrain cytotoxicity via PGE_2-mediated immune regulation

Authors

Xiong Zhu, Jie Wang, Xiaoxia Wang, ..., Juan Zhou, Yi Wang, Quanyi Wang

Correspondence

wangjie2018m@163.com (J.W.), wildwolf0101@163.com (Y.W.), wangqy@bjcdc.org (Q.W.)

In brief

Health sciences

Zhu et al., 2026, iScience 29, 115769
May 15, 2026
https://doi.org/10.1016/j.isci.2026.115769

CellPress

iScience

CellPress
OPEN ACCESS

Article

Single-cell transcriptomics reveals pediatric immune responses to COVID-19 vaccination

Xiong Zhu,[1,8] Jie Wang,[2,8,*] Xiaoxia Wang,[1,8] Zhaomin Feng,[3,4,8] Linglong Wan,[2,8] Lin Sun,[5,8] Jin Fu,[2] Fei Xiao,[2] Xiaolan Huang,[2] Nan Jia,[2] Min Chen,[2] Juan Zhou,[2] Yi Wang,[2,6,7,*] and Quanyi Wang[3,4,9,*]

[1]Central and Clinical Laboratory of Sanya People's Hospital, Sanya, Hainan 572000, People's Republic of China
[2]Experimental Research Center, Capital Center for Children's Health, Capital Medical University, Capital Institute of Pediatrics, Beijing 100020, P.R. China
[3]Beijing Key Laboratory of Surveillance, Early Warning and Pathogen Research on Emerging Infectious Diseases, Beijing Research Center for Respiratory Infectious Diseases, Beijing Center for Disease Prevention and Control, Beijing 100013, P.R. China
[4]School of Public Health, Capital Medical University, Beijing 100069, P.R. China
[5]Department of Endocrinology of Sanya People's Hospital, Sanya, Hainan 572000, People's Republic of China
[6]Molecular Diagnostic Center, Capital Center for Children's Health, Capital Medical University, Capital Institute of Pediatrics, Beijing 100020, P.R. China
[7]Beijing Research Center for Respiratory Infectious Disease, Beijing 100020, P.R. China
[8]These authors contributed equally
[9]Lead contact
*Correspondence: wangjie2018m@163.com (J.W.), wildwolf0101@163.com (Y.W.), wangqy@bjcdc.org (Q.W.)
https://doi.org/10.1016/j.isci.2026.115769

SUMMARY

Inactivated vaccines are critical to COVID-19 immunization, yet the cellular and molecular mechanisms driving pediatric responses warrant detailed characterization. We use single-cell transcriptomics to delineate the immune landscape of peripheral blood mononuclear cells in children vaccinated with CoronaVac. We uncovered a two-phase program: the primary dose establishes a memory foundation via expansion of survival-programmed memory B cells and a shift in $CD8^+$ T cells toward stress adaptation. The booster triggers an effector response marked by plasma cell differentiation, class-switching, and a pan-B cell type I interferon signature. Concurrently, vaccination reprograms monocytes into a pro-inflammatory, antigen-presenting state enriched for interferon-stimulated genes. This activation is counterbalanced by expanded myeloid-derived suppressor cells and *FOXP3*$^+$ regulatory T cells, which employ PGE_2 signaling to restrain excessive cytotoxicity and orchestrate helper T cell differentiation. Together, our atlas demonstrates that pediatric immunity to inactivated vaccines is tightly orchestrated, balancing antiviral programs with regulatory mechanisms to ensure safe protection.

INTRODUCTION

Coronavirus disease 2019 (COVID-19), caused by severe acute respiratory syndrome coronavirus 2 (SARS-CoV-2), has posed an unprecedented challenge to global public health since emerging in late 2019. As of 2025, the pandemic has resulted in an estimated 7.1 million deaths and over 778 million confirmed cases worldwide.[1] While children typically experience milder acute disease than adults, a significant number have required hospitalization, and a subset develop severe post-infectious complications such as multisystem inflammatory syndrome in children (MIS-C).[2–4] This underscores the need for effective prophylactic strategies tailored to this age group. Although therapeutic strategies such as antiviral agents and monoclonal antibodies have been developed, their efficacy is limited and largely dependent on the disease-stage, highlighting the critical role of vaccination in preventing COVID-19.[5,6]

A diverse array of vaccines have been developed using various technological platforms, including mRNA vaccines (BNT162b2 and mRNA-1273),[7] self-amplifying mRNA (sa-mRNA; ARCT-154),[8] viral vector (ChAdOx1 nCoV-19, Ad26.COV2.S, and Ad5-nCoV),[9] protein subunit (NVX-CoV2373 and ZF2001),[10,11] and inactivated virus (CoronaVac and BBIBP-CorV) vaccines.[12] Among these, CoronaVac, which is a two-dose, β-propiolactone-inactivated, aluminium-adjuvanted vaccine, is one of the most widely administered globally, particularly in China and many low- and middle-income countries, due to its favorable safety profile, convenient storage requirements, and proven effectiveness against severe disease.[12–15]

While clinical trials and longitudinal cohort studies have consistently demonstrated that COVID-19 vaccines elicit robust and durable immune responses across different age groups, mechanistic studies have predominantly focused on mRNA vaccines, elucidating pathways of antibody maturation and the dynamics of antigen-specific cellular responses.[14,16–21] In contrast,

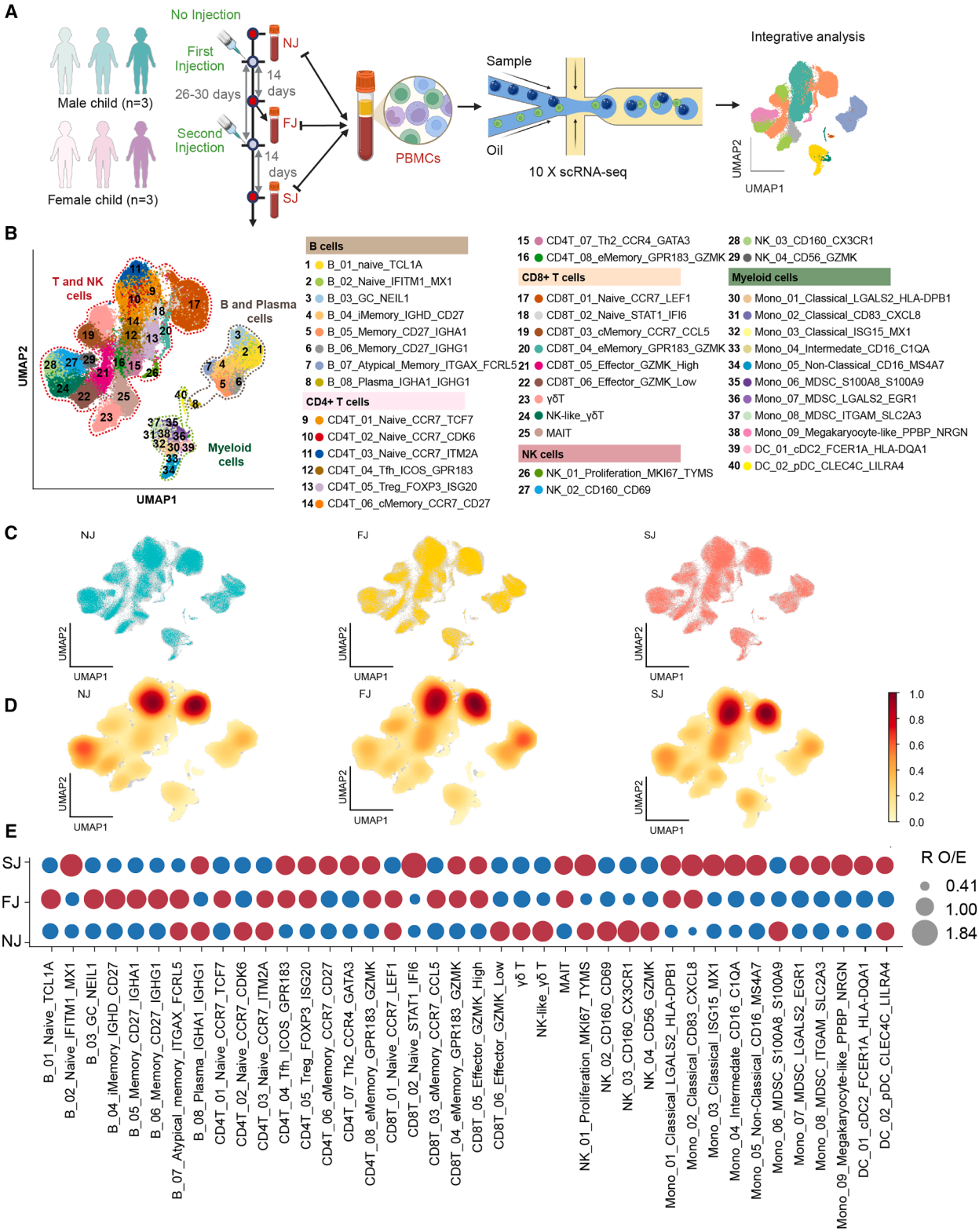

(legend on next page)

the immunological mechanisms of inactivated SARS-CoV-2 vaccines remain less thoroughly investigated. Recently, single-cell transcriptomic analyses have begun to characterized peripheral immune alterations following inactivated vaccination in specific populations, such as individuals with adverse reactions,[22] patients with rheumatoid arthritis,[23] and older adults,[24] revealing distinct immune remodeling patterns shaped by host-specific factors and age-related immunosenescence. Complementing these findings, Dou et al. specifically investigated the dynamic T cell evolution after inactivated SARS-CoV-2 vaccination, identifying robust activation of $CD8^+$ mucosal-associated invariant T (MAIT) cells and marked *KLRD1* upregulation, indicative of enhanced cytotoxic potential and antiviral preparedness.[25] Furthermore, studies comparing the peripheral immune landscape in adults after inactivated vaccination with that of natural SARS-CoV-2 infection found that the vaccine induces a milder yet coordinated immune activation, characterized by distinct antigen-specific cellular phenotypes (e.g., HLA class II^+ and $IL21R^+$ naive B cells) and unique pathway engagement (e.g., IL-15 receptor signaling).[26–28] Understanding these mechanisms in children is particularly crucial, as the pediatric immune system is still developing and exhibits distinct characteristics compared with that of adults. These differences can lead to unique vaccine response profiles, including variations in immunogenicity, efficacy, and the durability of protection. However, the cellular and molecular immune responses to inactivated vaccines (e.g., CoronaVac) in children remain poorly understood.

Here, we implemented single-cell RNA sequencing (scRNA-seq) to comprehensively profile peripheral blood mononuclear cells (PBMCs) from children vaccinated with CoronaVac. Samples were collected at three time points: before vaccination (Day 0), 9–13 days after the first dose, and 13–14 days after the second dose (Figure 1A). Our study provides a high-resolution longitudinal map of the transcriptomic changes in PBMCs following CoronaVac immunization and offers insights into the protective immunity generated by inactivated COVID-19 vaccines in a pediatric population.

RESULTS

A single-cell atlas of PBMCs during pediatric COVID-19 vaccination

To characterize the immunological landscape in children receiving the inactivated COVID-19 vaccine (CoronaVac), we profiled the transcriptomes of PBMCs using droplet-based single-cell RNA sequencing (scRNA-seq, 10× Genomics). Longitudinal PBMC samples were collected from six children before and after vaccination (Figure 1A). Samples were designated as no injection (NJ; pre-vaccination), first injection (FJ; ∼14 days post-first dose), and second injection (SJ; ∼14 days post-second dose) (Figure 1A; detailed metadata in Table S1). After removing low-quality cells and potential doublets, 142,195 high-quality cells (mean of 4,920 unique molecular identifiers [UMIs] and 1,697 genes per cell) were retained for downstream analysis, comprising 46,549 cells (32.7%) from the NJ group, 48,352 cells (34.0%) from the FJ group, and 47,294 cells (33.3%) from the SJ group (Figure S1).

Uniform manifold approximation and projection (UMAP) analysis of the integrated dataset revealed nine major immune cell populations based on canonical marker genes (Figures S2A and S2B).[28] These included B cells, plasma cells, $CD4^+$ T cells, $CD8^+$ T cells, γδ T cells, mucosal-associated invariant T (MAIT) cells, natural killer (NK) cells, monocytes, and dendritic cells (DCs). The UMAP visualization showed a clear separation of lymphoid and myeloid lineages (Figure S2A). To achieve higher cellular resolution, these populations were further subclustered into 40 distinct cell states based on canonical markers and differentially expressed genes (DEGs), comprising eight $CD4^+$ T cell subsets, nine $CD8^+$ T cell subsets (including γδ T cells, NK-like γδ T cells, and MAIT cells), four NK cell subsets, nine monocyte subsets, and two DC subsets (Figure 1B and Table S2). Projection of NJ, FJ, and SJ cells onto the UMAP revealed vaccination stage-associated shifts in transcriptional profiles and cellular distribution across immune lineages and states (Figures 1C and S2C). Density distribution analyses supported post-vaccination redistribution, with prominent activation of B cells, monocytes, and a subset of $CD4^+$ T cells (Figure 1D). Overall, this high-resolution single-cell PBMC atlas provides a comprehensive reference for dissecting the transcriptional dynamics of vaccine-induced immunity in children.

Comparative analysis revealed striking, vaccination-dependent shifts in PBMC composition. Relative to NJ group, the proportion of B cells increased after the first dose, while monocyte proportions expanded following both doses (Figures S2D–S2F). Furthermore, while the overall proportion of $CD8^+$ T cells remained stable, we observed an expansion of $CD4^+$ T and MAIT cells alongside a concurrent reduction in both NK and γδ T cells (Figures S2D–S2F), indicative of a robust transition toward an adaptive immune response. The frequency of plasma cells did not markedly increase after the first dose, a finding that may

Figure 1. A single-cell atlas of pediatric PBMCs following COVID-19 vaccination

(A) Schematic of the study design. Peripheral blood mononuclear cells (PBMCs) were collected from six children (three male, three female) at three time points: before vaccination (no injection, NJ), 9–13 after the first dose (first injection, FJ), and 13–14 days after the second dose (second injection, SJ). Isolated PBMCs were profiled using 10× genomics single-cell RNA sequencing (scRNA-seq), followed by integrative computational analysis.

(B) Uniform Manifold Approximation and Projection (UMAP) visualization of 142,195 integrated PBMCs from all samples, colored by 40 distinct cell subsets. Major cell lineages (B and plasma cells, T, and NK cells, myeloid cells) are demarcated by dashed lines. The key on the right lists the identified subsets, grouped by major cell type.

(C) UMAP visualization of integrated PBMCs colored by vaccination time point: NJ (blue), FJ (yellow), and SJ (red).

(D) Density plots showing the distribution of cells from each time point (NJ, FJ, and SJ) on the UMAP embedding. The color scale represents normalized cell density, with red indicating higher density.

(E) Dot plot illustrating the relative changes in cell subset proportions after vaccination. The ratio of observed to expected ($R_{O/E}$) frequencies is shown for the first injection (FJ) and second injection (SJ) groups relative to the no injection (NJ) group. Color and size of the dots represent the $R_{O/E}$ value, with red indicating enrichment ($R_{O/E} > 1$) and blue indicating depletion ($R_{O/E} < 1$) of a given cell subset.

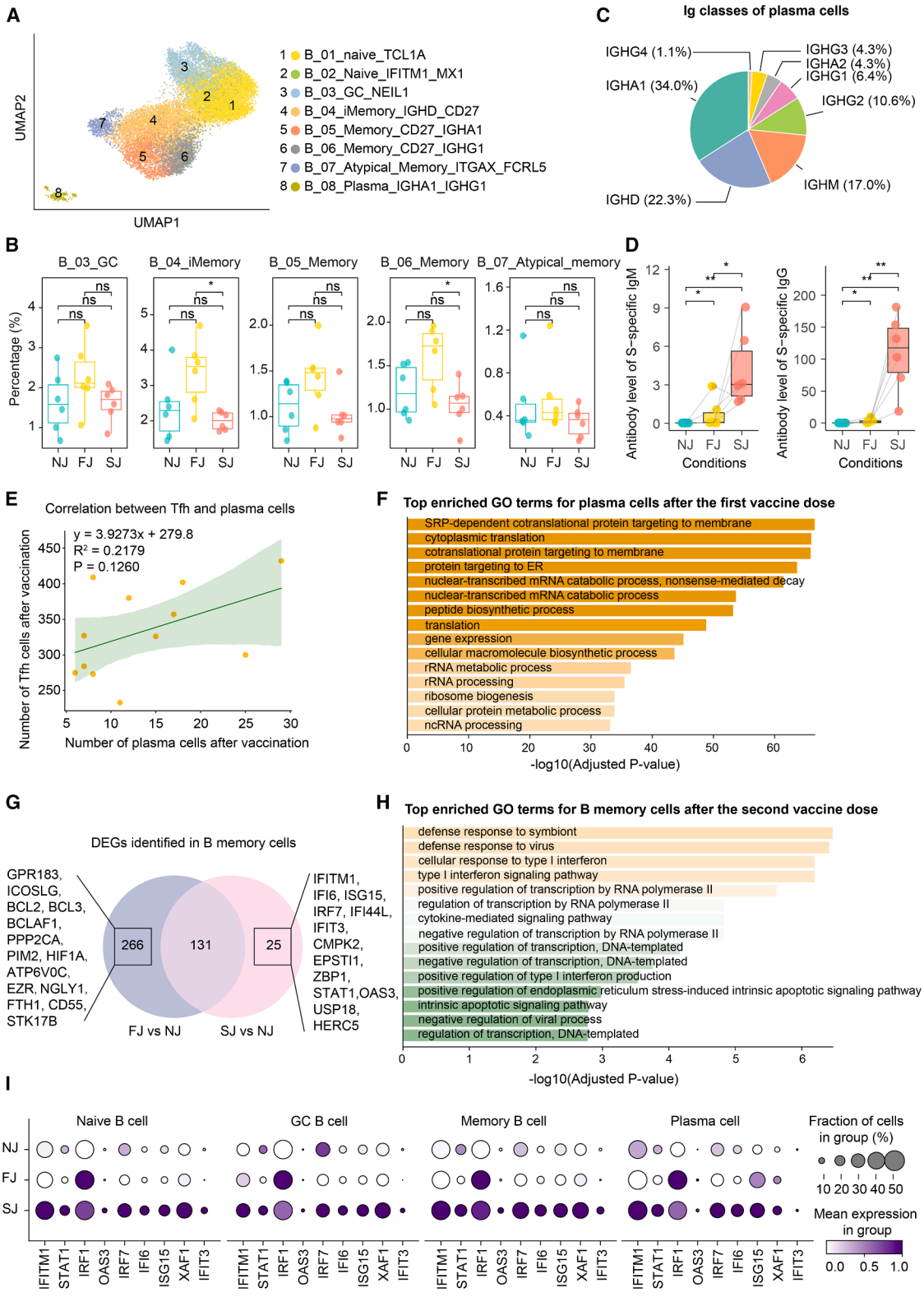

Figure 2. Vaccination induces a biphasic B cell response characterized by memory formation and interferon-driven plasma cell differentiation

(A) UMAP visualization of re-clustered B and plasma cells, colored by eight identified subsets.

(legend continued on next page)

reflect a need for prolonged antigen stimulation or that plasma cell levels had contracted by the sampling time point (Figure S2E). Analysis at the subset level using the ratio of observed-to-expected ($R_{O/E}$) further confirmed the previous findings (Figure 1E). In contrast, the second dose was characterized by the relative enrichment of plasma cells, most $CD4^+$ T cell subsets, and multiple monocyte subsets. Together, these findings delineate distinct immunological signatures for the priming and booster phases of vaccination in children, with the former establishing an adaptive memory foundation and the latter launching a robust, myeloid-supported effector response.

Distinct B cell fates and transcriptional programs define priming and booster responses

Re-clustering of B and plasma cells identified seven transcriptionally distinct populations, including naive, germinal center (GC), intermediate memory, and memory B cells, as well as IgA^+ and IgG^+ plasma cells (Figures 2A and S3A, and Table S2). Following the primary dose, GC and memory B cells tended to expand, indicative of B cell activation that prioritized memory formation over immediate large-scale antibody secretion (Figures 1E and 2B). In contrast, the booster dose led to an overrepresentation of plasma cells, despite no significant increase in their overall proportion (Figures 1E and S3B). These vaccine-induced plasma cells expression high levels of genes encoding immunoglobulin constant regions, including IgG1, IgG2, IgA1, IgA2, and IgM (Figures 2C and S3C), consistent with their role in secreting antigen-specific antibodies.[26,29] This transcriptional signature indicated enhanced SARS-CoV-2-specific humoral immunity, supported by serological evidence of increased neutralizing antibody titers after the booster dose (Figure 2D). Compared with the primary dose, *IGHM* was downregulated while *IGHA1* upregulated, indicating immunoglobulin class-switch recombination and response maturation with potential mucosal enhancement (Figure S3C). In parallel, plasma cell frequencies showed a positive trend of association with Tfh cell abundance in PBMCs (Figures 2E and S3D), suggesting a potential coordination between T and B cell responses. This aligns with prior evidence that Tfh cells are essential for high-affinity antibody production.[30,31]

To define the molecular programs of plasma cells following vaccination, we compared their transcriptomes from the FJ and SJ groups with those from the NJ group. DGE analysis identified 173 upregulated genes in plasma cells after the first dose compared with the pre-vaccination state, including antigen presentation (e.g., *HLA-DRA*, *HLA-DRB1*, and *CD74*) genes and AP-1 (*JUND*, *FOS*) and NF-κB (*NFKBIA*) components, reflecting an activated transcriptional program (Table S4). Concurrently, pronounced upregulation of numerous ribosomal protein genes and IgM heavy chain (*IGHM*) suggested enhanced translational machinery and a cellular state primed for large-scale antibody synthesis. GO analysis of these DGEs further indicated that plasma cells had entered a high-output antibody production state in response to the inactivated COVID-19 vaccine, evidenced by enrichment in pathways associated with protein synthesis and ribosome biogenesis (e.g., cytoplasmic translation, co-translational protein targeting to the membrane, RNA processing, etc) (Figure 2F and Table S4). In contrast, only three genes were upregulated in plasma cells after the second dose relative to the pre-vaccinated state (Table S4). This discrepancy is likely attributed to the sampling time point (∼14 days post-boost), as secondary immune responses are typically rapid, and plasma cell transcriptional activity may have already peaked and declined.

To characterize earlier stages of the B cell response, we examined transcriptomic alterations in memory B cells. DGE analysis identified 397 genes upregulated after the first dose and 156 after the second (Figure 2G and Table S5). Following the primary dose, memory B cells specifically upregulated survival- and activation-related genes (e.g., *BCL2*, *BCL3*, and *ICOSLG*) and showed enrichment in pathways governing transcriptional regulation, cellular stress responses, and apoptosis, indicating that primary immunization triggers transcriptional remodeling to establish the memory phenotype (Table S5). Booster immunization was associated with enrichment of antiviral and type I interferon pathways (Figure 2H), with increased expression of interferon-stimulated genes (e.g., IFITM1, ISG15, and IRF7) and their regulatory transcription factors (STAT1, IRF1, and IRF7) in memory B cells (Figure 2I). Notably, this transcriptional signature was consistently observed across all B cell subsets, including

(B) Boxplots showing the percentage of select B cell subsets (germinal center-like, intermediate memory, memory, and atypical memory) within the total B cell/plasma cell compartment across vaccination time points (NJ, FJ, SJ; $n = 6$ children per group). Each dot represents an individual donor. Boxes show the median and interquartile range (IQR), and whiskers extend to 1.5 times the IQR. Statistical significance was determined by a two-sided Wilcoxon rank-sum test; ns, not significant; $^*p < 0.05$.

(C) Pie chart illustrating the relative expression of different immunoglobulin heavy chain constant region genes within the plasma cell population after the second vaccine dose (SJ group), indicating class-switching.

(D) Boxplots depicting serum levels of SARS-CoV-2 Spike (S)-specific IgM (left) and IgG (right) neutralizing antibodies at the three time points ($n = 6$ children per group). Statistical significance was determined by a two-sided Wilcoxon signed-rank test; $^*p < 0.05$, $^{**}p < 0.01$.

(E) Scatterplot showing the positive correlation between the number of plasma cells and T follicular helper (Tfh) cells in PBMCs after vaccination (pooled FJ and SJ samples, $n = 12$). The green line represents the linear regression fit, with the 95% confidence interval shaded. The coefficient of determination (R^2) and P-value from linear regression are indicated.

(F) Gene Ontology (GO) enrichment analysis of genes upregulated in plasma cells after the first dose (FJ vs. NJ). The top biological process terms are shown, ranked by adjusted *p* value.

(G) Venn diagram illustrating the overlap of upregulated differentially expressed genes (DEGs) in memory B cells after the first dose (FJ vs. NJ) and the second dose (SJ vs. NJ). Representative genes are listed for each category.

(H) GO enrichment analysis of genes upregulated in memory B cells after the second dose (SJ vs. NJ). The top biological process terms are shown.

(I) Dot plot showing the expression of key interferon-stimulated genes (ISGs) and transcription factors across B cell subsets at each vaccination time point. Dot size indicates the fraction of cells expressing the gene, and color intensity represents the mean expression level in expressing cells.

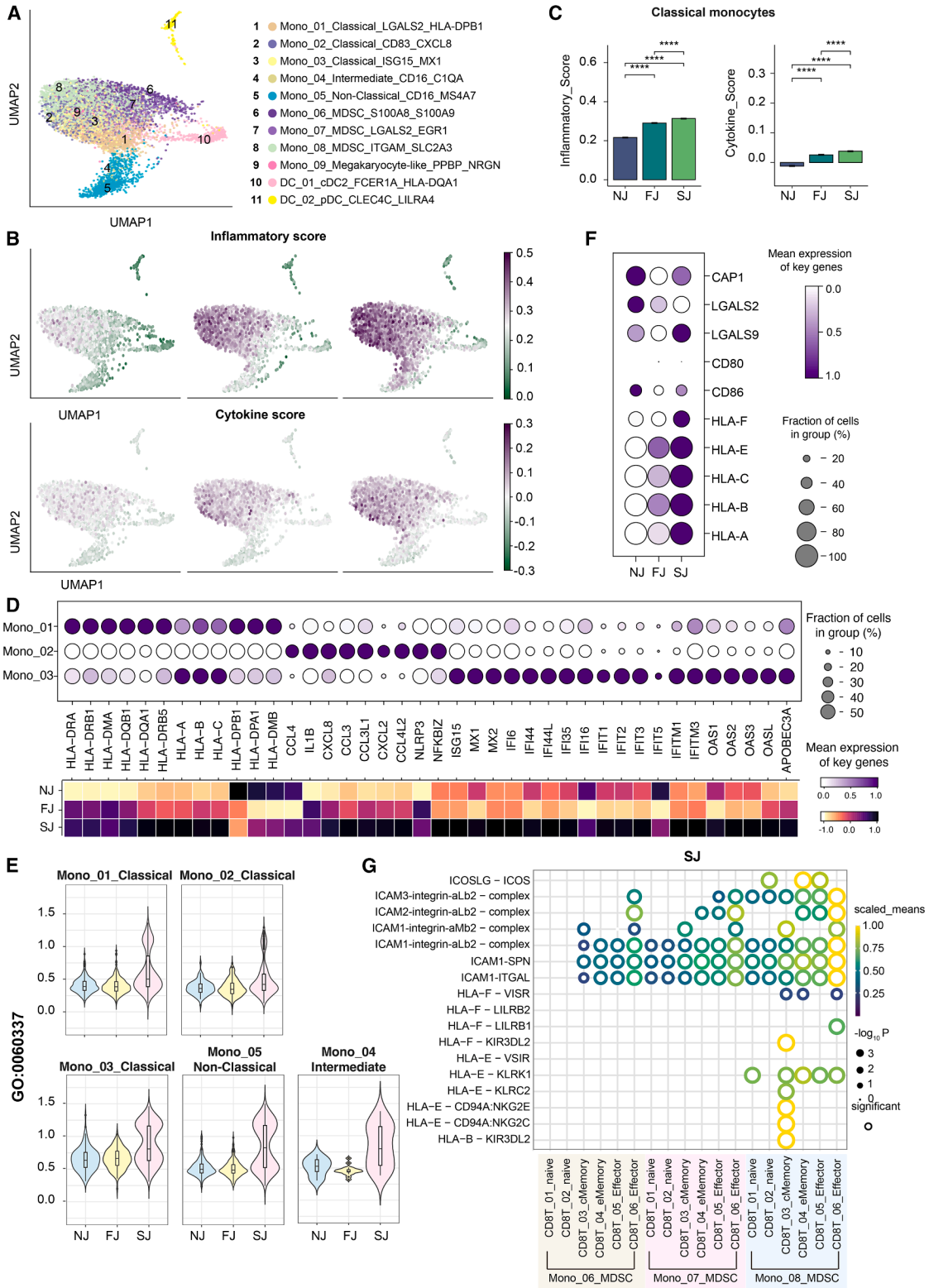

Figure 3. CoronaVac reprograms monocytes toward a pro-inflammatory, antigen-presenting state balanced by regulatory MDSCs

(A) UMAP visualization of re-clustered myeloid cells, identifying 11 distinct subsets including monocytes, myeloid-derived suppressor cells (MDSCs), and dendritic cells (DCs).

(legend continued on next page)

naive B cells and plasma cells (Figures 2I and S3F). These results indicate that booster immunization elicits a broad, systemic type I interferon response within the B cell compartment, placing even antigen-inexperienced naive B cells and terminally differentiated plasma cells in a heightened antiviral state. Such global IFN responsiveness may contribute to immediate antiviral defense and influence subsequent B cell activation and differentiation.

Together, COVID-19 vaccination elicits a biphasic B cell response: priming expands a survival-programmed memory pool, while the booster generates class-switched plasma cells and potent neutralizing antibodies. Moreover, the booster also triggers a pan-B cell type I interferon response, fostering a broad antiviral state.

CoronaVac vaccination reprograms pediatric myeloid immunity toward a balanced antiviral and regulatory state

Given the marked expansion of monocytes after vaccination (Figure 1), we next delineated vaccine-induced alterations within the myeloid compartment in pediatric PBMCs. High-resolution re-clustering of myeloid cells resolved 11 distinct subsets, including monocytes and DCs (Figures 3A, S4A, and Table S2). Monocytes were partitioned into nine subsets: three classical (Mono_01–03), intermediate (Mono_04), non-classical (Mono_05), three myeloid-derived suppressor cell (MDSC) (Mono_06–08), and megakaryocyte-like subsets (Mono_09). The Mono_09 subset, previously described in other inflammatory contexts,[32,33] displayed a transcriptional profile highly similar to that of megakaryocytes (e.g., *PPBP*, *PF4*, *SRGN*), suggesting a potential role in modulating chronic inflammation and influencing monocyte differentiation. DCs were subdivided into type 2 conventional DCs (DC_01) and plasmacytoid DCs (DC_02). cDC1s were not detected, likely due to their low abundance in peripheral blood, despite their well-established role in priming cytotoxic T cell responses.[34] After the first CoronaVac dose, expansion was largely confined to the Mono_02_Classical population, whereas the second dose was associated with broader trends toward increased representation across multiple monocyte subsets (Figures 1E and S4B). Notably, the DC_02_pDC population progressively declined after vaccination, consistent with reports in SARS-CoV-2 infection[35] (Figure S4B).

Given the central role of monocytes in inflammation, we profiled vaccination-induced inflammatory and cytokine gene expression programs using curated gene sets (Table S3). Monocytes exhibited the highest response scores among all cell types (Figures S4C and S4D). Subset-level analysis further revealed distinct pro-inflammatory cytokine expression patterns, including genes encoding *S100A8/9/12* and *CXCL2/8/16* (Figure S4E). Moreover, inflammatory activation progressively increased from the first to the second vaccine dose across all monocyte subsets (Figures 3B, 3C, and S5A). The mono_02_-classical and mono_09_megakaryocyte-like subsets exhibited markedly elevated cytokine scores, with *IL1B*, *S100A12*, *CXCL8*, *CCL3*, and *CCL3L1* as the top five contributors (Figures S4D and S5B). These cytokines are central mediators of innate immunity: *IL1B* and *S100A12* amplify inflammatory signaling, *CXCL8* recruits neutrophils, and *CCL3*/*CCL3L1* direct monocyte and lymphocyte chemotaxis. Together, their induction highlights potent pro-inflammatory programs triggered by vaccination, which may underlie the transient, low-grade fever commonly observed in children post-immunization.

We next examined the functional polarization of classical monocyte subsets. Mono_01 was enriched for antigen-presentation genes (e.g., *HLA-DRA*, *HLA-DRB1/5*, *HLA-A/B/C*), mono_02 for pro-inflammatory mediators (e.g., *CCL4*, *IL1B*, *CXCL8*, and *CCL3*), and Mono_03 for interferon-stimulated genes (e.g., *ISG15*, *MX1/2*, *IFI6*, *IFI44*, and *IFIT2*). This heterogeneity underscores their distinct roles in orchestrating vaccine-induced immunity by simultaneously amplifying antiviral programs and promoting $CD4^+$/$CD8^+$ T cell priming through enhanced MHC-I/II-mediated antigen presentation (Figure 3D). These signatures were further amplified after the second vaccine dose, reflecting enhanced innate immune activation and intercellular communication (Figure 3D). DEG analysis of classical monocytes further revealed 433 and 372 upregulated genes in the FJ and SJ groups, respectively, with 102 genes uniquely induced after the second dose, including *IFITM3*, *IFITM2*, *ISG15*, and *CCL3*. These SJ-specific gene were enriched in type I interferon responses, antiviral defense, and cytokine-mediated innate pathways (Figure S5C and Table S6).

A similar transcriptional reprogramming was evident in non-classical (mono_05) and intermediate (mono_04) monocyte subsets. Although mono_05 frequencies remained stable, they exhibited a marked increase in type I interferon signatures after the second dose (Figure 3E and Table S7). The intermediate subset, the primary source of C1 complement components, maintained stable *C1QA/B/C* levels (logFC <0.5) following vaccination but also showed strong induction of type I interferon programs (Figures 3E and S5D). These findings demonstrate

(B) UMAP plots of myeloid cells colored by module scores for inflammation (top) and cytokine production (bottom), showing dose-dependent increases.
(C) Bar charts quantifying the mean inflammatory (top) and cytokine (bottom) scores specifically within classical monocytes at each time point ($n = 6$). Error bars represent s.e.m. Statistical significance was determined by a two-sided Student's t tests; $^{**}p < 0.01$, $^{****}p < 0.0001$.
(D) Top, dot plot illustrating the expression of key functional genes distinguishing the three classical monocyte subsets: antigen presentation (mono_01), pro-inflammatory (mono_02), and interferon-stimulated (mono_03). Bottom, heatmap showing the mean expression of these genes in all classical monocytes at baseline (NJ) and after the second dose (SJ).
(E) Violin plots showing the module score for the "type I interferon signaling pathway" (GO:0060337) in classical (mono_01, mono_02, and mono_03), non-classical (mono_05), and intermediate (mono_04) monocyte subsets across time points.
(F) Dot plot depicting the expression of key antigen presentation (HLA class I and II) and co-stimulatory/inhibitory molecules in classical monocytes, showing dose-dependent upregulation.
(G) Dot plot of selected ligand-receptor interactions between MDSC subsets (mono_06, _07, _08) and $CD8^+$ T cell subsets after the second vaccine dose (SJ). Dot color indicates the scaled mean expression of the interacting pair; dot size represents statistical significance (-log10 p value). Significant interactions ($p < 0.05$) are marked with a black border.

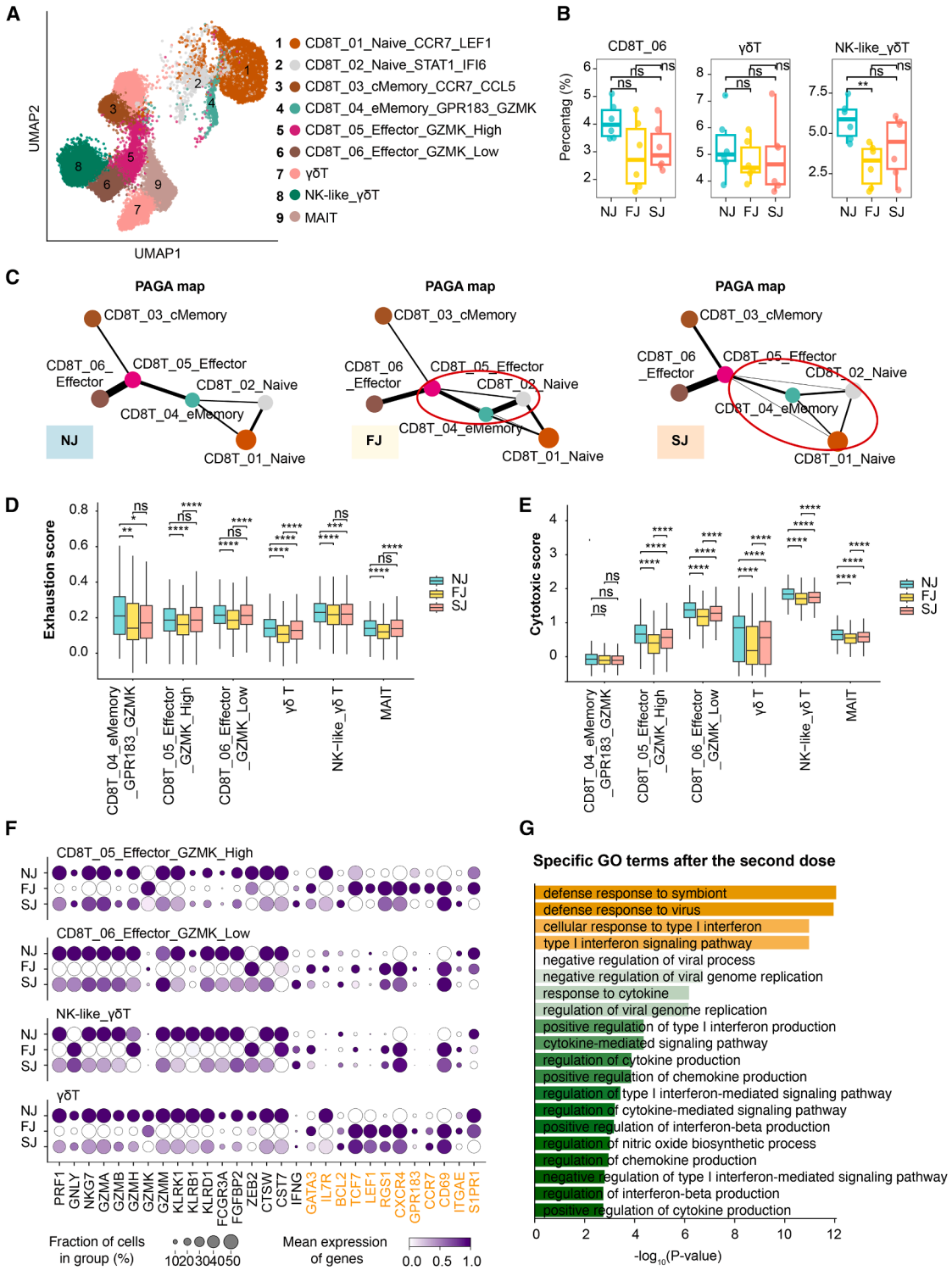

Figure 4. Sequential vaccination drives a functional shift in CD8⁺ T cells from stress adaptation to reinforced antiviral immunity

(A) UMAP visualization of re-clustered CD8⁺ T cells, including innate-like T cells (γδ T, MAIT), colored by nine identified subsets.

(B) Boxplots showing the percentage of CD8T_06, γδT, and NK-lile γδT populations within the total cells across vaccination time points (NJ, FJ, SJ; *n* = 6 children per group). Boxes indicate the median and interquartile range (IQR), and whiskers extend to 1.5 times the IQR. ns, not significant (two-sided Wilcoxon rank-sum test).

(legend continued on next page)

that CoronaVac vaccination drives a coordinated transcriptional reprogramming of monocytes toward an interferon-enriched, antigen-presenting phenotype that bridges innate activation with adaptive T cell priming.

We identified three MDSC subsets characterized by markedly reduced *HLA-DR* expression and elevated levels of the alarmins *S100A8/A9* and *S100A12* (Figures 3A, S4A, and S5E), consistent with previously reported transcriptional signatures of suppressive myeloid cells.[36] Despite diminished HLA-DR expression, these MDSC subsets retained intermediate levels of MHC-I molecules (*HLA-A/B/C/E/F*), which were upregulated in a dose-dependent manner (Figure 3F). Ligand-receptor analysis further revealed robust MHC-I-mediated communication between $CD8^+$ T cells and the mono_08_MDSC subset after second dose, including inhibitory interactions (*HLA-E/F-VSIR*, *HLA-B/F-KIR3DL2*) that may promote immune tolerance,[37,38] and activating pairs (*HLA-E-KLRK1, HLA-E-CD94:NKG2C/E*) that could enhance cytotoxic responses (Figures 3G and S6).[39–41] Vaccination also induced ICOSLG-ICOS and ICAM1/2/3-integrin interactions between MDSCs and naive $CD8^+$ T cells, supporting the formation of immune synapses and potential T cell activation (Figures 3G and S6).[42,43] Nevertheless, the overall transcriptional program of these MDSCs were consistent with a suppressive phenotype. The concomitant low expression of co-stimulatory molecules (e.g., *CD86*) and a booster-induced galectin shift, marked by *LGALS2* downregulation and *LGALS9* upregulation, suggest that these cells preferentially drive T cell anergy, exhaustion, or apoptosis rather than productive activation (Figures 3F and 3G).[44]

Collectively, our study demonstrates that CoronaVac vaccination remodels the pediatric myeloid landscape through a dose-dependent expansion and transcriptional reprogramming of monocytes. These cells are primed with enhanced inflammatory, interferon, and antigen-presentation programs that bridge innate sensing with T cells activation. Concurrently, expanded MDSC subsets acquire the capacity to engage T cells but are programmed to restrain excessive activation, ensuring a balanced and controlled protective immunity in children.

Sequential vaccination reshapes pediatric $CD8^+$ T cell programs from stress adaptation to reinforced antiviral immunity

Based on canonical markers and DEGs, we identified nine distinct $CD8^+$ T cell subsets, including six conventional $CD8^+$ T cell and three innate-like T cell populations (MAIT, γδ T, and NK-like γδ T) (Figures 4A, S7A, and Table S2). MAIT and γδ T cells were included because they express CD8A and CD8B (Figures S2B and S7A). Broadly, we categorized the conventional $CD8^+$ T cell populations into two naive (CD8T_01–02), one central memory (CD8T_03), one effector memory (CD8T_04) and two effector T subpopulations (Figures 4A, S7A, and Table S2).

After the first dose, cMemory $CD8^+$ T cells showed a trend toward expansion consistent with memory establishment, whereas interferon-responsive naive CD8T_02 subset (marked by *STAT1* and *IFI6*) was relatively enriched after the second dose, implying rapid interferon mobilization upon boosting (Figure S7B). Concurrently, $GZMK^+$ CD8T_eMemory, $GZMK^+$ CD8T_effector, and MAIT cells exhibited apparent increases across both doses, while highly cytotoxic subsets—$GZMK^-GZMB^+PRF1^+$ CD8T effectors and two $GZMB^+PRF1^+$ γδ T cell populations—showed a tendency toward reduction, implying a bias toward low-cytotoxic, proinflammatory effector activity in the pediatric vaccine response (Figures 4B, S7A, and S7B).

We performed partition-based graph abstraction (PAGA) analysis to examine the developmental trajectories of the six conventional $CD8^+$ T subclusters (Figures 4C and S7C). The PAGA map identified CD8T_04_eMemory and CD8T_05_Effector as highly connected nodes, acting as intermediates linking naive (CD8T_01/02_naive) and central memory (CD8T_03_cMemory) populations to more activated and highly cytotoxic $CD8^+$ T cell subclusters (e.g., CD8T_06_effector). Following the first vaccine dose, connectivity increased between CD8T_02_naive and CD8T_04_eMemory/CD8T_05_effector, consistent with a trajectory from interferon-activated naive cells toward effector-like differentiation. Upon the second dose, CD8T_05_effector displayed even stronger connectivity with other $CD8^+$ T cell subclusters, highlighting its central role in amplifying cytotoxic potential during booster response.

Analysis of exhaustion and cytotoxicity signatures, using previously defined gene sets, revealed heterogeneous functional states among $CD8^+$ T cell subsets (Figures S7D, S7E, and Table S3). Effector and innate-like $CD8^+$ T cells exhibited higher exhaustion scores, implying greater functional impairment upon sustained antigenic stimulation (Figure S7D). Compared to the pre-vaccination baseline, CD8T_06_effector and innate-like $CD8^+$ T cells, which declined in frequency after the first vaccine dose, also displayed reduced exhaustion scores (Figure 4D). This likely reflects the contraction phase, during which highly cytotoxic and terminally exhausted clones either undergo apoptosis or migrate out of circulation, leaving behind a less exhausted, lower-cytotoxic population in peripheral blood. Accordingly, effector $CD8^+$ cytotoxic activity declined after

(C) Partition-based graph abstraction (PAGA) maps illustrating the connectivity between conventional $CD8^+$ T cell subsets at each time point. Nodes represent cell subsets, and line thickness indicates connectivity strength. Red circles highlight key developmental trajectories emerging after the first (FJ) and second (SJ) doses.

(D and E) Boxplots comparing exhaustion (D) and cytotoxicity (E) module scores in effector and innate-like $CD8^+$ T cell subsets across the three time points ($n = 6$). Statistical significance was determined by a two-sided Student's *t* tests; ns, not significant; $^{**}p < 0.01$, $^{***}p < 0.001$, $^{****}p < 0.0001$.

(F) Dot plot displaying the expression of key genes related to cytotoxicity (black), survival and memory (purple), and tissue residency (orange) in effector and innate-like $CD8^+$ T cell subsets. Data are shown for each time point. Dot size represents the fraction of cells expressing the gene; color intensity indicates the mean expression level.

(G) Gene Ontology (GO) enrichment analysis of genes upregulated in effector $CD8^+$ T cells after the second dose (SJ vs. NJ). Top biological process terms are shown, ranked by adjusted *p* value.

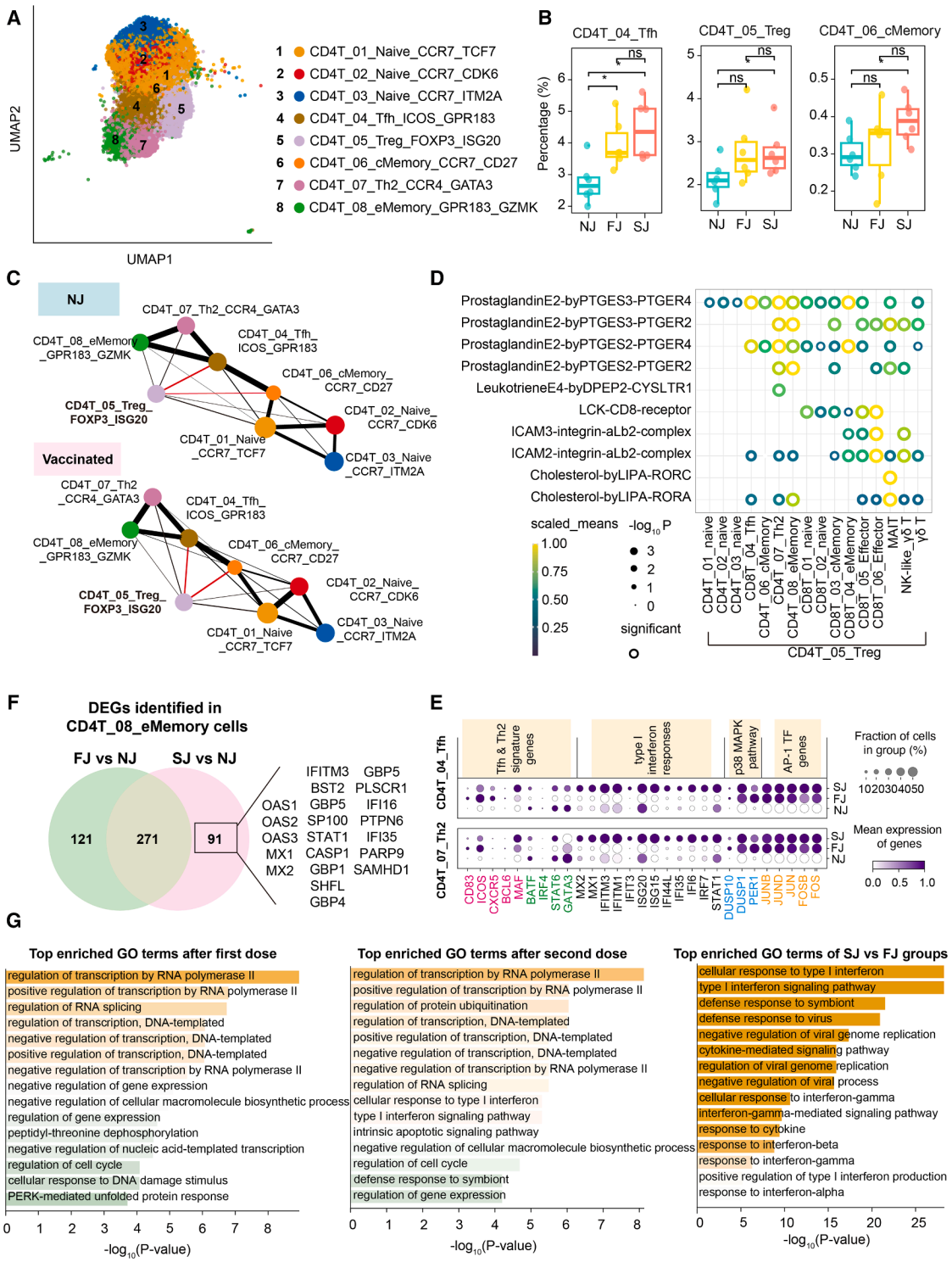

Figure 5. Treg-mediated PGE_2 signaling orchestrates $CD4^+$ T cell differentiation and effector programs after vaccination

(A) UMAP visualization of re-clustered $CD4^+$ T cells, colored by eight identified subsets.

(B) Boxplots showing the percentage of CD4T_04_Tfh, CD4T_05_Treg, and CD4T_06_cMemory populations within the total cells across vaccination time points (NJ, FJ, SJ; $n = 6$ children per group). Boxes indicate the median and interquartile range (IQR); whiskers extend to 1.5 times the IQR. ns, not significant; $^*p < 0.05$ (two-sided Wilcoxon rank-sum test).

(legend continued on next page)

vaccination, with reduced cytotoxic molecule expression (Figures 4E, 4F, and S7F) and increased programs linked to survival (GATA3, IL7R, BCL2, TCF7, and LEF1), homing (RGS1, CXCR4, GPR183, and CCR7), and tissue residency (CD69 and ITGAE). These findings suggest that by ~14 days post-vaccination, a substantial fraction of effector CD8$^+$ T cells may be transitioning toward memory-precursor or tissue-resident states, thereby supporting durable immunity while limiting vaccine-associated immunopathology in children.

To further investigate the transcriptional profiles of effector CD8$^+$ T cells, we analyzed DEGs and conducted GO enrichment. Compared with the pre-vaccination baseline, 378 genes were upregulated after the first vaccine dose and 285 after the second, with 211 shared (Figure S7G and Table S8), indicating substantial vaccine-induced reprogramming. At approximately day 14 after the first dose, effector CD8$^+$ T cells showed enrichment for pathways related to transcriptional and post-transcriptional regulation, metabolic adaptation, cytokine signaling (including IL-4 and IL-7, which promote memory differentiation), and regulation of cell-death rather than a dominant cytotoxic signature. These features indicate a transcriptional landscape reflecting a stress-adaptation program coupled with divergent cell fates, wherein a subset of effector CD8$^+$ T cells engages survival and memory-forming trajectories, while others undergo contraction or apoptosis to maintain immune homeostasis (Figure S7G and Table S8). In contrast, after the second dose, effector CD8$^+$ T cells exhibited enrichment for antiviral defense, type I interferon signaling, and cytokine/chemokine regulatory pathways (Figure 4G and Table S8), reflecting an amplified antiviral and inflammatory response. Together, these findings highlight a dynamic shift in effector CD8$^+$ T cell programs from stress-adaptation and fate determination after the priming dose to reinforced antiviral immunity upon booster vaccination.

Treg-mediated PGE_2 signaling orchestrates coordinated CD4$^+$ T cell differentiation and humoral immunity

Analysis of the CD4$^+$ T cell compartment identified four major populations: naive T cells (CD4T_01–03), helper T cells (CD4T_04 and CD4T_07), memory CD4$^+$ T cells (CD4T_06 and CD4T_08), and regulatory T cells (CD4T_05) (Figures 5A, S8A, and Table S2). Although the three naive CD4$^+$ T cell subsets all expressed canonical naive markers (e.g., CCR7, TCF7, and LEF1), they displayed distinct expression patterns of these genes (Figure S8A). The CD4T_02_naive cluster expressed high levels of cell cycle-related genes (e.g., *CDK6*, *PIM1*), indicating a quiescent population poised for rapid expansion upon antigenic stimulation. The frequency of naive CD4$^+$ T cells showed a decreasing trend, whereas memory, helper, and regulatory CD4$^+$ T cell subsets increased significantly (Figures 1E, 5B, and S8B), suggesting a shift toward an activated, antigen-experienced landscape.

Trajectory inference mapped a continuum from naive CD4$^+$ T cells to central memory, which bifurcated toward either Tfh/Th2 lineages—supporting B cell help and humoral immunity—or effector memory, consistent with long-term memory formation (Figure 5C). Post-vaccination, the Treg subset (CD4T_05) displayed broad connectivity across the CD4$^+$ T cell network, with enhanced interactions observed with Tfh and central memory populations (Figure 5C). Ligand-receptor analysis further revealed that Tregs engage prostaglandin E_2 (PGE_2) signaling and *ICAM2/3-integrin* $\alpha L\beta 2$ pathway to modulate multiple CD4$^+$ T cell subsets (CD4T_04_Tfh, CD4T_06_cMemory, CD4T_07_Th2), and CD8$^+$ T cell populations (e.g., memory and effector CD8$^+$ T subsets, and innate-like subsets) (Figures 5D and S8C). Prior studies has shown that PGE_2 signaling via the Gs-coupled receptors PTGER2 and PTGER4 activates the adenylate cyclase-cAMP-PKA-CREB pathway, which can attenuate type I inflammatory activity and promote a shift toward Th2- and B cell-dominated humoral immunity.[45] In this context, our results suggest that Tregs may use PGE_2-mediated signaling to tune the balance between cytotoxic inflammation and helper programs, supporting a coordinated shift toward humoral immunity following vaccination.

Concurrently, both helper CD4$^+$ T cell subsets (CD4T_07_Th2 and CD4T_04_Tfh) expanded and underwent pronounced transcriptional reprogramming after vaccination. DEG analysis revealed upregulation of AP-1 signaling (e.g., *JUN* and *FOS*), p38MAPK signaling (e.g., *PER1*, *DUSP10*, and *DUSP1*) and type I interferon responses (e.g., *STAT1*, *IRF7*, *IFI6*, and *ISG15*) (Figure 5E and Table S9), consistent with antigen-driven antiviral activation. GO term enrichment analysis corroborated these findings, identifying enriched pathways associated with "defense response to virus," "cytokine response," and "regulation of gene expression," indicating a coordinated antiviral response (Figures S8D, S8E, and Table S9). Importantly, key Tfh regulators and markers, such as *BCL6*, *MAF*, and the surface molecules *CXCR5*, *ICOS*, and *CD83*, were upregulated after the first vaccination (Figure 5E), reflecting rapid acquisition of follicular positioning and B cell help potential. Key lineage-specifying transcription factors for Th2 and Tfh differentiation (e.g., *GATA3*, *STAT6*, *IRF4*, and *BATF*) were transiently downregulated after

(C) Partition-based graph abstraction (PAGA) maps illustrating the connectivity between CD4$^+$ T cell subsets at baseline (NJ, top) and after vaccination (vaccinated, bottom). Nodes represent cell subsets, and line thickness indicates connectivity strength, highlighting enhanced Treg interactions post-vaccination.
(D) Dot plot of selected ligand-receptor interactions originating from regulatory T cells (CD4T_05_Treg) and targeting other T cell subsets after the second vaccine dose (SJ). Dot color indicates the scaled mean expression of the interacting pair; dot size represents statistical significance (-log10 p value). Significant interactions ($p < 0.05$) are marked with a black border.
(E) Dot plot displaying the expression of key genes related to T cell activation and function in helper T cell subsets (Tfh and Th2) across vaccination time points. Genes are grouped by functional pathways (Tfh & Th2 signature, type I interferon responses, p38MAPK, AP-1). Dot size represents the fraction of cells expressing the gene; color intensity indicates mean expression.
(F) Venn diagram showing the overlap of upregulated differentially expressed genes (DEGs) in effector memory CD4$^+$ T cells (CD4T_08_eMemory) after the first (FJ vs. NJ) and second (SJ vs. NJ) doses. Representative genes for each category are listed.
(G) Gene ontology (GO) enrichment analysis of upregulated DEGs in effector memory CD4$^+$ T cells. Bar charts show the top biological process terms after the first dose (left), after the second dose (middle), and for genes uniquely upregulated after the second dose (SJ vs. FJ, right).

the first dose but rebounded after the second dose, suggesting consolidation of Th2/Tfh programs upon the second antigen exposure (Figure 5E).

Effector memory CD4$^+$ T cell population (CD4T_08_eMemory) also exhibited alterations in response to vaccine stimulation (Figure S8B and Table S10). This subset was characterized by high expression of cytotoxic genes (*GZMK*, *GZMA*, and *GNLY*) and S100-family genes (e.g., *S100A4/A6/A10/A11*), indicating a poised effector state with enhanced migratory and cytolytic capacity for rapid antiviral responses (Figure S8A and Table S2). Relative to baseline, this subset showed 392 and 362 genes upregulated after the first and second doses, respectively, with an overlap of 271 genes (Figure 5F and Table S10). GO analysis revealed these upregulated genes were significantly enriched in gene-regulation pathways and ER stress-associated unfolded protein response, reflecting antigen-driven transcriptional and post-transcriptional regulation, as well as stress adaptation (Figure 5G and Table S10). By contrast, the booster uniquely enriched interferon-γ and antiviral programs, indicating a booster-specific consolidation of an IFN-imprinted effector-memory state.

In summary, vaccination drove the differentiation of naive CD4$^+$T cells into helper subsets specialized for B cell support and into GZMK$^+$ effector-memory populations with antiviral potential. Concurrently, FOXP3$^+$ Tregs exerted regulatory control through *PGE$_2$-PTGER2/4* and *ICAM*-dependent communication.

DISCUSSION

The COVID-19 pandemic highlights the urgent need to understand vaccine-induced immunity across all age groups, particularly in children, whose developing immune systems exhibit unique response dynamics. Here, we provide a high-resolution single-cell atlas of the pediatric immune response to an inactivated vaccine, revealing a distinct, two-phase immunological program driven by the prime-boost regimen. Our study demonstrates that the primary dose initiates a fundamental shift from innate to adaptive immunity, characterized by expanding foundational B cell memory subsets and CD4$^+$ T cells, and reducing innate-like NK and γδ T cells. This initial phase appears to prioritize establishing a durable memory framework rather than mounting an immediate, large-scale effector response. In contrast, the booster dose triggers a robust effector phase, marked by significant enrichment of antibody-secreting plasma cells and a broad expansion of activated monocyte subsets. This demarcation between priming and boosting (memory formation followed by a potent, myeloid-supported effector activation) highlights a tightly regulated and sequential process. While previous studies have largely focused on mRNA vaccines in adults,[16–18] our work provides the first detailed cellular map demonstrating how an inactivated vaccine systematically and safely builds protective immunity in children. This biphasic model, which balances memory formation with controlled effector function, likely contributes to the vaccine's favorable safety and efficacy profile in this pediatric population.

This biphasic response is particularly evident within the B cell lineage, where priming and boosting orchestrate distinct cellular fates and transcriptional programs. The primary dose establishes a crucial foundation by expanding a pool of memory B cells transcriptionally programmed for survival, as evidenced by upregulating genes such as *BCL2* and *BCL3*. This strategic prioritization of memory formation over immediate, large-scale antibody secretion ensures generating a durable immunological scaffold. Interestingly, such early memory B cell expansion was not observed in our previous adult study sampling at 21 days post-first dose, suggesting that B cell expansion may occur within an early, temporally restricted window that was not captured at the adult sampling time point.[26] Upon this foundation, the booster dose unleashes a potent effector response, driving the differentiation of class-switched plasma cells correlating with a sharp rise in neutralizing antibody titers. This maturation of the humoral response, which includes a notable shift toward IgA production, suggests inducing immunity with potential mucosal benefits. A striking observation is the emergence of a pan-B cell type I interferon (IFN) signature after the booster. In contrast to mRNA- and adenoviral-vectored vaccines, where IFN responses have been primarily attributed to monocytes or activated T cells,[16,46,47] the IFN activation observed here spans even naive and memory B cell subsets, indicating that the inactivated-vaccine adjuvant creates a broad antiviral state that extends beyond antigen-specific clones. Such an IFN-rich milieu may lower the activation threshold for subsequent B cell responses and contribute to immediate, non-specific protection. Thus, the CoronaVac regimen effectively programs pediatric B cells first for longevity and recall potential, then for a powerful, IFN-supercharged effector phase, ensuring both the depth and breadth of protective humoral immunity.

The observed robust humoral immunity is supported by a profound and coordinated reprogramming of the myeloid compartment, which serves as both an accelerator and a brake on the vaccine response. Following vaccination, pediatric monocytes undergo a dose-dependent expansion and functional polarization, acquiring a potent pro-inflammatory and antigen-presenting phenotype, consistent with our previous observations in adults and other vaccines (ChAdOx1 nCoV-19 and BNT162b2).[16,26,46] The booster dose, in particular, amplifies this effect, enriching classical monocytes with a strong type I interferon signature and enhancing expression of MHC class I and II molecules. These reprogramming positions monocytes as central hubs that bridge innate sensing with adaptive immunity, fueling T cell priming and shaping the antiviral milieu required for B cell maturation. Concurrently, our analysis reveals a sophisticated counter-regulatory mechanism: expanding myeloid-derived suppressor cell (MDSC) populations. These MDSCs, while upregulating MHC-I for T cell engagement, are transcriptionally poised for immune suppression and characterized by low HLA-DR expression and a galectin signature favoring T cell energy. Notably, such MDSC populations were not annotated in our previous adult study,[26] pointing to potential age-related differences in immunoregulatory strategies. In pediatric individuals, myeloid-mediated suppressive programs may be more readily engaged to counterbalance vaccine-induced inflammatory activation, thereby preventing excessive immunopathology. Overall, this duality (powerful innate activation balanced by robust myeloid-mediated suppression) is a key feature of the pediatric response to CoronaVac, likely underpinning the

vaccine's ability to elicit strong protection while maintaining a high safety profile.

This carefully calibrated balance between activation and regulation extends deeply into the T cell compartment, where an interplay between helper, effector, and regulatory lineages ensures a potent yet controlled response. Vaccination drives the differentiation of naive $CD4^+$ T cells along two critical trajectories: one toward Tfh and Th2 helper subsets essential for orchestrating B cell maturation and class-switching, and another toward $GZMK^+$ effector-memory cells poised for rapid antiviral action. This differentiation is accompanied by strong transcriptional signatures of activation, including AP-1 and type I interferon signaling, reflecting their engagement within the pro-inflammatory milieu created by myeloid cells. Of note, an increase in Tfh cells was observed at $\sim$ day 14 after the first dose in children, but not in our previously reported adult cohort sampled at day 21. This contrast may also reflect age- and/or sampling time-dependent differences in the kinetics of $CD4^+$ T cell helper responses, with a potentially earlier and/or more transient Tfh response during primary immunization (26).

This $CD4^+$ T cell activation program is, however, governed by an expanded population of $FOXP3^+$ regulatory T cells. Our data reveal that these Tregs function as central conductors and employ PGE_2 signaling via the *PTGER2/4* axis to communicate broadly with both $CD4^+$ and $CD8^+$ T cell subsets. This PGE_2-mediated signaling is known to dampen cytotoxic, type I inflammatory responses while promoting humoral immunity,[45] and our findings suggest this is a key mechanism for fine-tuning the pediatric vaccine response. This regulatory oversight is clearly reflected in the $CD8^+$ T cell compartment, which undergoes a biphasic transcriptional trajectory. The primary dose prompts a program of stress adaptation and memory precursor formation, and a contraction of highly cytotoxic clones. The booster then reinforces antiviral potential, but within a framework that prioritizes sustained immunity over immediate, exhaustive cytotoxicity. Within this regulatory context, the transcriptionally restrained cytotoxic state of $CD8^+$ T cells may provide a molecular framework for the relatively modest and rapidly waning CTL responses reported after two-dose inactivated SARS-CoV-2 vaccination, which should be further examined by dedicated functional assays. Together, this reveals an orchestrated T cell program where Treg-mediated PGE_2 signaling shapes both helper T cell function and restrains $CD8^+$ effector activity, ensuring the development of effective, multi-faceted cellular immunity without inducing excessive inflammation.

In conclusion, our longitudinal single-cell atlas provides an unprecedented high-resolution map of the pediatric immune response to an inactivated COVID-19 vaccine, revealing a precisely orchestrated, two-phase program. The primary dose establishes a durable adaptive memory foundation by expanding survival-programmed memory B cells and conditioning T cells for stress adaptation. The booster then unleashes a potent, IFN-driven effector response, characterized by class-switched plasma cells and pro-inflammatory, antigen-presenting monocytes. This robust activation is counterbalanced by expanded myeloid-derived suppressor cells and Treg-mediated PGE_2 signaling, which restrain excessive cytotoxicity and ensure immune homeostasis. These findings not only illuminate the cellular basis for the efficacy and safety of inactivated vaccines in children but also provide a mechanistic framework to guide the rational design of future pediatric immunization strategies.

Limitations of the study

While this study provides key insights into pediatric vaccine immunity, it is important to acknowledge several limitations. First, our analysis was restricted to peripheral blood, which only indirectly reflects the foundational immunological events, such as GC reactions, occurring within secondary lymphoid organs. Second, the modest cohort size may limit the generalizability of our findings, and validation in larger, more diverse pediatric populations is required. Third, neutralizing antibody titers and antigen-specific cytotoxic T lymphocyte (CTL) responses were not assessed, limiting our ability to link transcriptional immune programs with functional correlates of protective immunity. Finally, single-cell transcriptomic analyses performed at discrete time points provide only an inferential snapshot of cellular states and dynamics, which should be further corroborated by multi-omic approaches and direct functional assays (such as serum PGE_2 quantification and pathway-specific validation experiments).

RESOURCE AVAILABILITY

Lead contact

Further information and requests for resources should be directed to and will be fulfilled by the lead contact, Jie Wang (wangjie2018m@163.com).

Materials availability

This study did not generate new unique reagents.

Data and code availability

- The scRNA-seq data reported in this paper have been deposited in the OMIX database at the China National Center for Bioinformation (CNCB) Beijing Institute of Genomics, Chinese Academy of Sciences, under OMIX: OMIX014455. The accession number is also listed in the key resources table.
- Custom data analysis scripts used in this study are included in the supplemental information.
- Any additional information required to reanalyze the data reported in this paper is available from the lead contact upon request.

ACKNOWLEDGMENTS

We acknowledged the support received from Research Foundation of Capital Institute of Pediatrics (XZDX-2025-002), Beijing Research Center for Respiratory Infectious Diseases Project (BJRID2025-009), Innovation Platform for Academicians of Hainan Province, South China Sea Innovative Talents of Hainan Province, Sanya Talent Development Special Project, and Sanya High-Quality Backbone Talent Cultivation.

We gratefully acknowledge the participation of Beijing Digitf Biotechnology Co., Ltd. (Beijing) and Tongyuan Gene Co., Ltd. (Qingdao) for the support of cloud computing platform, and Analytical BioSciences Co., Ltd. (Beijing) for the support of construction of single cell sequencing Library, and thanks Dr. Yunke Li (Beijing Digitf Biotechnology), Miss. RanRan Gao (Analytical BioSciences), JuanJuan Yu (Analytical BioSciences), and Mr. Feng Zhu (Analytical BioSciences) for her contribution.

AUTHOR CONTRIBUTIONS

Q.W. and Y.W. conceived the study. X.Z., J.W., X.W., Z.F., and L.S. supervised and controlled this project. X.Z., X.W., and L.W. collected and curated the

biological samples. L.S., J.F., F.X., X.H., N.J., M.C., and J.Z. performed the experiments. Y.W. and J.W. contributed to the analysis tools and performed the software. X.Z., J.W., and Y.W. drafted the original paper. Q.W. and Y.W. revised and edited this paper. Q.W., Y.W., X.Z., J.W., X.W., Z.F., and L.S. reviewed the paper. All authors have read and approved the article.

DECLARATION OF INTERESTS

The authors declare that they have no conflict of interest.

STAR★METHODS

Detailed methods are provided in the online version of this paper and include the following:

- KEY RESOURCES TABLE
- EXPERIMENTAL MODEL AND STUDY PARTICIPANT DETAILS
  - Volunteer cohort
- METHOD DETAILS
  - Sample collection and single-cell RNA sequencing
  - Data analysis and batch effect correction
  - Cell clustering and annotations
  - Identifying changes in immune cell proportion
  - Determining cell state scores
- QUANTIFICATION AND STATISTICAL ANALYSIS

SUPPLEMENTAL INFORMATION

Supplemental information can be found online at https://doi.org/10.1016/j.isci.2026.115769.

Received: November 18, 2025
Revised: January 21, 2026
Accepted: April 13, 2026
Published: April 15, 2026

REFERENCES

1. Organization, W.H. (2025). WHO COVID-19 Dashboard: Coronavirus (COVID-19) cases. https://data.who.int/dashboards/covid19/cases.
2. Yasuhara, J., Kuno, T., Takagi, H., and Sumitomo, N. (2020). Clinical characteristics of COVID-19 in children: A systematic review. Pediatr. Pulmonol. *55*, 2565–2575. https://doi.org/10.1002/ppul.24991.
3. Fernandes, D.M., Oliveira, C.R., Guerguis, S., Eisenberg, R., Choi, J., Kim, M., Abdelhemid, A., Agha, R., Agarwal, S., Aschner, J.L., et al. (2021). Severe Acute Respiratory Syndrome Coronavirus 2 Clinical Syndromes and Predictors of Disease Severity in Hospitalized Children and Youth. J. Pediatr. *230*, 23–31.e10. https://doi.org/10.1016/j.jpeds.2020.11.016.
4. Feldstein, L.R., Rose, E.B., Horwitz, S.M., Collins, J.P., Newhams, M.M., Son, M.B.F., Newburger, J.W., Kleinman, L.C., Heidemann, S.M., Martin, A.A., et al. (2020). Multisystem Inflammatory Syndrome in U.S. Children and Adolescents. N. Engl. J. Med. *383*, 334–346. https://doi.org/10.1056/NEJMoa2021680.
5. Tabatabaei, S., Keykhaee, Z., Nooraei, S., Ayati, M., Behzadmand, M., Azimi, S., Eskati, F., and Ahmadian, G. (2025). SARS-CoV-2 and Coronaviruses: Understanding Transmission, Impact, and Strategies for Prevention and Treatment. Drugs Drug Candidates *4*, 5. https://doi.org/10.3390/ddc4010005.
6. Murmu, N., Sarkar, M., Dey, S., Manna, R., Roy, S., Mondal, T., Halder, S., Bhattacharjee, N., Dash, S.K., and Giri, B. (2024). Efficacy and limitations of repurposed drugs and vaccines for COVID-19. J. Med. Surg. Public Health *2*, 100041. https://doi.org/10.1016/j.glmedi.2023.100041.
7. Park, J.W., Lagniton, P.N.P., Liu, Y., and Xu, R.H. (2021). mRNA vaccines for COVID-19: what, why and how. Int. J. Biol. Sci. *17*, 1446–1460. https://doi.org/10.7150/ijbs.59233.
8. (2024). First self-amplifying mRNA vaccine approved. Nat. Biotechnol. *42*, 4. https://doi.org/10.1038/s41587-023-02101-2.
9. Vanaparthy, R., Mohan, G., Vasireddy, D., and Atluri, P. (2021). Review of COVID-19 viral vector-based vaccines and COVID-19 variants. Infez. Med. *29*, 328–338. https://doi.org/10.53854/liim-2903-3.
10. Keech, C., Albert, G., Cho, I., Robertson, A., Reed, P., Neal, S., Plested, J.S., Zhu, M., Cloney-Clark, S., Zhou, H., et al. (2020). Phase 1-2 Trial of a SARS-CoV-2 Recombinant Spike Protein Nanoparticle Vaccine. N. Engl. J. Med. *383*, 2320–2332. https://doi.org/10.1056/NEJMoa2026920.
11. Dai, L., Zheng, T., Xu, K., Han, Y., Xu, L., Huang, E., An, Y., Cheng, Y., Li, S., Liu, M., et al. (2020). A Universal Design of Betacoronavirus Vaccines against COVID-19, MERS, and SARS. Cell *182*, 722–733.e11. https://doi.org/10.1016/j.cell.2020.06.035.
12. Khoshnood, S., Arshadi, M., Akrami, S., Koupaei, M., Ghahramanpour, H., Shariati, A., Sadeghifard, N., and Heidary, M. (2022). An overview on inactivated and live-attenuated SARS-CoV-2 vaccines. J. Clin. Lab. Anal. *36*, e24418. https://doi.org/10.1002/jcla.24418.
13. Zhang, M.X., Zhang, T.T., Shi, G.F., Cheng, F.M., Zheng, Y.M., Tung, T.H., and Chen, H.X. (2021). Safety of an inactivated SARS-CoV-2 vaccine among healthcare workers in China. Expert Rev. Vaccines *20*, 891–898. https://doi.org/10.1080/14760584.2021.1925112.
14. Hu, L., Sun, J., Wang, Y., Tan, D., Cao, Z., Gao, L., Guan, Y., Jia, X., and Mao, J. (2023). A Review of Inactivated COVID-19 Vaccine Development in China: Focusing on Safety and Efficacy in Special Populations. Vaccines (Basel) *11*, 1045. https://doi.org/10.3390/vaccines11061045.
15. Mallapaty, S. (2021). China's COVID vaccines have been crucial - now immunity is waning. Nature *598*, 398–399. https://doi.org/10.1038/d41586-021-02796-w.
16. Arunachalam, P.S., Scott, M.K.D., Hagan, T., Li, C., Feng, Y., Wimmers, F., Grigoryan, L., Trisal, M., Edara, V.V., Lai, L., et al. (2021). Systems vaccinology of the BNT162b2 mRNA vaccine in humans. Nature *596*, 410–416. https://doi.org/10.1038/s41586-021-03791-x.
17. De Pasquale, C., Drommi, F., Calabrò, A., Botta, C., Sidoti Migliore, G., Carrega, P., Vento, G., Gaeini, A., Pezzino, G., Freni, J., et al. (2025). BNT162b2 COVID-19 vaccination elicits the expansion of CD16(+)CD8(+) T cells endowed with natural killer cell features. J. Allergy Clin. Immunol. *155*, 1981–1992. https://doi.org/10.1016/j.jaci.2025.01.024.
18. Borcherding, N., Kim, W., Quinn, M., Han, F., Zhou, J.Q., Sturtz, A.J., Schmitz, A.J., Lei, T., Schattgen, S.A., Klebert, M.K., et al. (2024). CD4(+) T cells exhibit distinct transcriptional phenotypes in the lymph nodes and blood following mRNA vaccination in humans. Nat. Immunol. *25*, 1731–1741. https://doi.org/10.1038/s41590-024-01888-9.
19. Jara, A., Undurraga, E.A., Zubizarreta, J.R., González, C., Acevedo, J., Pizarro, A., Vergara, V., Soto-Marchant, M., Gilabert, R., Flores, J.C., et al. (2022). Effectiveness of CoronaVac in children 3-5 years of age during the SARS-CoV-2 Omicron outbreak in Chile. Nat. Med. *28*, 1377–1380. https://doi.org/10.1038/s41591-022-01874-4.
20. Jara, A., Undurraga, E.A., Flores, J.C., Zubizarreta, J.R., González, C., Pizarro, A., Ortuño-Borroto, D., Acevedo, J., Leo, K., Paredes, F., et al. (2023). Effectiveness of an inactivated SARS-CoV-2 vaccine in children and adolescents: a large-scale observational study. Lancet Reg. Health, Am. *21*, 100487. https://doi.org/10.1016/j.lana.2023.100487.
21. Zhang, Y., Zeng, G., Pan, H., Li, C., Hu, Y., Chu, K., Han, W., Chen, Z., Tang, R., Yin, W., et al. (2021). Safety, tolerability, and immunogenicity of an inactivated SARS-CoV-2 vaccine in healthy adults aged 18-59 years: a randomised, double-blind, placebo-controlled, phase 1/2 clinical trial. Lancet Infect. Dis. *21*, 181–192. https://doi.org/10.1016/S1473-3099(20)30843-4.
22. Jiang, M., Yu, H., Luo, L., Zhang, L., Xiong, A., Wang, J., Wang, Q., Liu, Y., Liu, S., Xiong, Y., et al. (2023). Single cell characteristics of patients with vaccine-related adverse reactions following inactivated COVID-19

vaccination. Hum. Vaccin. Immunother. *19*, 2246542. https://doi.org/10.1080/21645515.2023.2246542.

23. Fan, Y., Huang, S., Wu, D., Chu, M., Zhao, J., Zhang, J., Wang, Y., Gui, Y., Ye, X., Wang, G., et al. (2024). Immune features revealed by single-cell RNA and single-cell TCR/BCR sequencing in patients with rheumatoid arthritis receiving COVID-19 booster vaccination. J. Med. Virol. *96*, e29573. https://doi.org/10.1002/jmv.29573.

24. Xiao, C., Ren, Z., Zhang, B., Mao, L., Zhu, G., Gao, L., Su, J., Ye, J., Long, Z., Zhu, Y., et al. (2023). Insufficient epitope-specific T cell clones are responsible for impaired cellular immunity to inactivated SARS-CoV-2 vaccine in older adults. Nat. Aging *3*, 418–435. https://doi.org/10.1038/s43587-023-00379-0.

25. Dou, X., Peng, M., Jiang, R., Li, W., and Zhang, X. (2023). Upregulated CD8(+) MAIT cell differentiation and KLRD1 gene expression after inactivated SARS-CoV-2 vaccination identified by single-cell sequencing. Front. Immunol. *14*, 1174406. https://doi.org/10.3389/fimmu.2023.1174406.

26. Wang, Y., Wang, X., Luu, L.D.W., Li, J., Cui, X., Yao, H., Chen, S., Fu, J., Wang, L., Wang, C., et al. (2022). Single-cell transcriptomic atlas reveals distinct immunological responses between COVID-19 vaccine and natural SARS-CoV-2 infection. J. Med. Virol. *94*, 5304–5324. https://doi.org/10.1002/jmv.28012.

27. He, S., Liu, S.Q., Teng, X.Y., He, J.Y., Liu, Y., Gao, J.H., Wu, Y., Hu, W., Dong, Z.J., Bei, J.X., and Xu, J.H. (2024). Comparative single-cell RNA sequencing analysis of immune response to inactivated vaccine and natural SARS-CoV-2 infection. J. Med. Virol. *96*, e29577. https://doi.org/10.1002/jmv.29577.

28. Zhang, Y., Guo, X., Li, C., Kou, Z., Lin, L., Yao, M., Pang, B., Zhang, X., Duan, Q., Tian, X., et al. (2021). Transcriptome Analysis of Peripheral Blood Mononuclear Cells in SARS-CoV-2 Naive and Recovered Individuals Vaccinated With Inactivated Vaccine. Front. Cell. Infect. Microbiol. *11*, 821828. https://doi.org/10.3389/fcimb.2021.821828.

29. Dunn-Walters, D., Townsend, C., Sinclair, E., and Stewart, A. (2018). Immunoglobulin gene analysis as a tool for investigating human immune responses. Immunol. Rev. *284*, 132–147. https://doi.org/10.1111/imr.12659.

30. Crotty, S. (2019). T Follicular Helper Cell Biology: A Decade of Discovery and Diseases. Immunity *50*, 1132–1148. https://doi.org/10.1016/j.immuni.2019.04.011.

31. Xiao, K., Cao, Y., Yan, P., Hu, Y., Luu, L.D.W., Pan, P., Gu, H., Duan, Z., Wang, J., Chen, W., et al. (2025). A Large-Scale Single-Cell Atlas Reveals the Peripheral Immune Panorama of Bacterial Pneumonia. Am. J. Respir. Crit. Care Med. *211*, 2363–2381. https://doi.org/10.1164/rccm.202501-0217OC.

32. Yao, J., Liu, T., Zhao, Q., Ji, Y., Bai, J., Wang, H., Yao, R., Zhou, X., Chen, Y., and Xu, J. (2023). Genetic landscape and immune mechanism of monocytes associated with the progression of acute-on-chronic liver failure. Hepatol. Int. *17*, 676–688. https://doi.org/10.1007/s12072-022-10472-y.

33. Hu, Y., Hu, Y., Xiao, Y., Wen, F., Zhang, S., Liang, D., Su, L., Deng, Y., Luo, J., Ou, J., et al. (2020). Genetic landscape and autoimmunity of monocytes in developing Vogt-Koyanagi-Harada disease. Proc. Natl. Acad. Sci. USA *117*, 25712–25721. https://doi.org/10.1073/pnas.2002476117.

34. Jongbloed, S.L., Kassianos, A.J., McDonald, K.J., Clark, G.J., Ju, X., Angel, C.E., Chen, C.J.J., Dunbar, P.R., Wadley, R.B., Jeet, V., et al. (2010). Human CD141+ (BDCA-3)+ dendritic cells (DCs) represent a unique myeloid DC subset that cross-presents necrotic cell antigens. J. Exp. Med. *207*, 1247–1260. https://doi.org/10.1084/jem.20092140.

35. Arunachalam, P.S., Wimmers, F., Mok, C.K.P., Perera, R.A.P.M., Scott, M., Hagan, T., Sigal, N., Feng, Y., Bristow, L., Tak-Yin Tsang, O., et al. (2020). Systems biological assessment of immunity to mild versus severe COVID-19 infection in humans. Science *369*, 1210–1220. https://doi.org/10.1126/science.abc6261.

36. Zhao, F., Hoechst, B., Duffy, A., Gamrekelashvili, J., Fioravanti, S., Manns, M.P., Greten, T.F., and Korangy, F. (2012). S100A9 a new marker for monocytic human myeloid-derived suppressor cells. Immunology *136*, 176–183. https://doi.org/10.1111/j.1365-2567.2012.03566.x.

37. Wang, L., Rubinstein, R., Lines, J.L., Wasiuk, A., Ahonen, C., Guo, Y., Lu, L.F., Gondek, D., Wang, Y., Fava, R.A., et al. (2011). VISTA, a novel mouse Ig superfamily ligand that negatively regulates T cell responses. J. Exp. Med. *208*, 577–592. https://doi.org/10.1084/jem.20100619.

38. Coles, M.C., McMahon, C.W., Takizawa, H., and Raulet, D.H. (2000). Memory CD8 T lymphocytes express inhibitory MHC-specific Ly49 receptors. Eur. J. Immunol. *30*, 236–244. https://doi.org/10.1002/1521-4141(200001)30:1<236::AID-IMMU236>3.0.CO;2-X.

39. Choi, S.J., Koh, J.Y., Rha, M.S., Seo, I.H., Lee, H., Jeong, S., Park, S.H., and Shin, E.C. (2023). KIR(+)CD8(+) and NKG2A(+)CD8(+) T cells are distinct innate-like populations in humans. Cell Rep. *42*, 112236. https://doi.org/10.1016/j.celrep.2023.112236.

40. Sottile, R., Panjwani, M.K., Lau, C.M., Daniyan, A.F., Tanaka, K., Barker, J.N., Brentjens, R.J., Sun, J.C., Le Luduec, J.B., and Hsu, K.C. (2021). Human cytomegalovirus expands a CD8(+) T cell population with loss of BCL11B expression and gain of NK cell identity. Sci. Immunol. *6*, eabe6968. https://doi.org/10.1126/sciimmunol.abe6968.

41. Moser, J.M., Gibbs, J., Jensen, P.E., and Lukacher, A.E. (2002). CD94-NKG2A receptors regulate antiviral CD8(+) T cell responses. Nat. Immunol. *3*, 189–195. https://doi.org/10.1038/ni757.

42. Dong, C., Juedes, A.E., Temann, U.A., Shresta, S., Allison, J.P., Ruddle, N.H., and Flavell, R.A. (2001). ICOS co-stimulatory receptor is essential for T-cell activation and function. Nature *409*, 97–101. https://doi.org/10.1038/35051100.

43. Staunton, D.E., Marlin, S.D., Stratowa, C., Dustin, M.L., and Springer, T.A. (1988). Primary structure of ICAM-1 demonstrates interaction between members of the immunoglobulin and integrin supergene families. Cell *52*, 925–933. https://doi.org/10.1016/0092-8674(88)90434-5.

44. Gossink, E.M., Coffer, P.J., Cutilli, A., and Lindemans, C.A. (2025). Immunomodulation by galectin-9: Distinct role in T cell populations, current therapeutic avenues and future potential. Cell. Immunol. *407*, 104890. https://doi.org/10.1016/j.cellimm.2024.104890.

45. Kalinski, P. (2012). Regulation of immune responses by prostaglandin E2. J. Immunol. *188*, 21–28. https://doi.org/10.4049/jimmunol.1101029.

46. Jin Choi, S., Lee, W., Cheol Kim, S., Jo, H.Y., Park, H.Y., Bin Kim, H., Park, W.Y., Ho Park, S., Ko, J.H., and Seok Lee, J. (2024). Longitudinal multiomic profiling and corticosteroid modulation of the immediate innate immune response to an adenovirus-vector vaccine. Vaccine *42*, 126118. https://doi.org/10.1016/j.vaccine.2024.07.019.

47. Cao, Q., Wu, S., Xiao, C., Chen, S., Chi, X., Cui, X., Tang, H., Su, W., Zheng, Y., Zhong, J., et al. (2021). Integrated single-cell analysis revealed immune dynamics during Ad5-nCoV immunization. Cell Discov. *7*, 64. https://doi.org/10.1038/s41421-021-00300-2.

48. Wang, Y., Sun, Q., Zhang, Y., Li, X., Liang, Q., Guo, R., Zhang, L., Han, X., Wang, J., Shao, L., et al. (2023). Systemic immune dysregulation in severe tuberculosis patients revealed by a single-cell transcriptome atlas. J. Infect. *86*, 421–438. https://doi.org/10.1016/j.jinf.2023.03.020.

49. Wang, Y., Luu, L.D.W., Liu, S., Zhu, X., Huang, S., Li, F., Huang, X., Guo, L., Zhang, J., Ge, H., et al. (2023). Single-cell transcriptomic analysis reveals a systemic immune dysregulation in COVID-19-associated pediatric encephalopathy. Signal Transduct. Target. Ther. *8*, 398. https://doi.org/10.1038/s41392-023-01641-y.

50. Wolock, S.L., Lopez, R., and Klein, A.M. (2019). Scrublet: Computational Identification of Cell Doublets in Single-Cell Transcriptomic Data. Cell Syst. *8*, 281–291.e9. https://doi.org/10.1016/j.cels.2018.11.005.

51. Ren, X., Wen, W., Fan, X., Hou, W., Su, B., Cai, P., Li, J., Liu, Y., Tang, F., Zhang, F., et al. (2021). COVID-19 immune features revealed by a large-scale single-cell transcriptome atlas. Cell *184*, 5838. https://doi.org/10.1016/j.cell.2021.10.023.

52. Korsunsky, I., Millard, N., Fan, J., Slowikowski, K., Zhang, F., Wei, K., Baglaenko, Y., Brenner, M., Loh, P.R., and Raychaudhuri, S. (2019). Fast, sensitive and accurate integration of single-cell data with Harmony. Nat. Methods *16*, 1289–1296. https://doi.org/10.1038/s41592-019-0619-0.

53. Hu, C., Li, T., Xu, Y., Zhang, X., Li, F., Bai, J., Chen, J., Jiang, W., Yang, K., Ou, Q., et al. (2023). CellMarker 2.0: an updated database of manually curated cell markers in human/mouse and web tools based on scRNA-seq data. Nucleic Acids Res. *51*, D870–D876. https://doi.org/10.1093/nar/gkac947.

54. Wolf, F.A., Hamey, F.K., Plass, M., Solana, J., Dahlin, J.S., Göttgens, B., Rajewsky, N., Simon, L., and Theis, F.J. (2019). PAGA: graph abstraction reconciles clustering with trajectory inference through a topology preserving map of single cells. Genome Biol. *20*, 59. https://doi.org/10.1186/s13059-019-1663-x.

55. Troulé, K., Petryszak, R., Cakir, B., Cranley, J., Harasty, A., Prete, M., Tuong, Z.K., Teichmann, S.A., Garcia-Alonso, L., and Vento-Tormo, R. (2025). CellPhoneDB v5: inferring cell-cell communication from single-cell multiomics data. Nat. Protoc. *20*, 3412–3440. https://doi.org/10.1038/s41596-024-01137-1.

56. Zhang, C., Li, J., Cheng, Y., Meng, F., Song, J.W., Fan, X., Fan, H., Li, J., Fu, Y.L., Zhou, M.J., et al. (2023). Single-cell RNA sequencing reveals intrahepatic and peripheral immune characteristics related to disease phases in HBV-infected patients. Gut *72*, 153–167. https://doi.org/10.1136/gutjnl-2021-325915.

STAR★METHODS

KEY RESOURCES TABLE

REAGENT or RESOURCE	SOURCE	IDENTIFIER
Biological samples		
Human peripheral blood (pediatric participants; EDTA-anticoagulated)	This study	N/A
Chemicals, peptides, and recombinant proteins		
HISTOPAQUE-1077	Sigma-Aldrich	Cat#10771
10× Red Blood Cell Lysis Solution	Miltenyi Biotec	Cat#130-094-183
1× Phosphate-buffered saline (PBS)	Gibco	Cat#10010023
Deposited data		
Single-cell RNA-seq of human PBMCs	This study	OMIX: OMIX014455
Software and algorithms		
kallisto/bustools	Open-source	Identifier: v0.24.4; URL: https://www.kallistobustools.org
anndata	Open-source	v0.7.6; URL: https://anndata.readthedocs.io
Scanpy	Open-source	v1.11.1; URL: https://scanpy.readthedocs.io
Scrublet	Open-source	URL: https://github.com/swolock/scrublet
Harmony	Open-source	URL: https://github.com/immunogenomics/harmon
CellPhoneDB	Open-source	URL: https://github.com/ventolab/CellphoneDB
Enrichr repository	Enrichr	URL: https://maayanlab.cloud/Enrichr/
Gene Ontology	GeneOntology.org	URL: https://geneontology.org
CellMarker 2.0 database	CellMarker 2.0	http://www.bio-bigdata.center/

EXPERIMENTAL MODEL AND STUDY PARTICIPANT DETAILS

Volunteer cohort

Three male and three female healthy children aged 11 years (n = 6) were admitted at Sanya People's Hospital and enrolled in the study. Peripheral blood samples were collected at three key timepoints (Figure 1A and Table S1): the pre-vaccination baseline (time point 1, Day 0); 9–13 days following the first dose (time point 2); and finally, 13–14 days following the second dose (time point 3). All six participants provided matched samples at all three time points. This study design allowed us to investigate the kinetics of the immune responses following both primary and secondary immunizations. This study was conducted in accordance with the Declaration of Helsinki and approved by the Ethics Committee of the Sanya People's Hospital (SYPH-2021-26).

METHOD DETAILS

Sample collection and single-cell RNA sequencing

Comprehensive cohort information is presented in Figure 1. Fresh blood samples collected at each time point were immediately processed for peripheral blood mononuclear cells (PBMCs) isolation using standard density gradient centrifugation. PBMCs are commonly used to evaluate immune-regulatory responses at the single-cell level. PBMCs were isolated using HISTOPAQUE-1077 (Sigma-Aldrich, Cat. No. 10771) according to the manufacturer's instructions. Briefly, 3 mL of fresh peripheral blood was collected into ethylenediaminetetraacetic acid (EDTA)–anticoagulated tubes and subsequently layered onto HISTOPAQUE-1077. After centrifugation, PBMCs remained at the plasma–HISTOPAQUE-1077 interface and were carefully transferred into a new tube. Residual erythrocytes were removed using 10× Red Blood Cell Lysis Solution (Miltenyi Biotec, Cat. No. 130-094-183), and the cells were washed twice with 1× phosphate-buffered saline (PBS) (Gibco, Cat. No. 10010023). Cell viability was assessed using a Countstar cell viability kit with viability exceeding 90%.[26]

The isolated PBMCs were subsequently loaded onto a Chromium Controller (10× Genomics) for cell encapsulation, during which individual cells were barcoded and partitioned into single-cell gel bead-in-emulsions (GEMs) using the Chromium Single Cell 5′ Gel Bead and Multiplex Kit and Chip Kit (10× Genomics), according to the manufacturer's instructions. mRNA captured within individual GEMs was reverse-transcribed into complementary DNA (cDNA), which was subsequently amplified. Single-cell RNA libraries were

prepared using the Chromium Single Cell 5′ Kit v2 (x10 Genomics; PN-1000263) according to the manufacturer's instructions and sequenced on an Illumina NovaSeq 6000 platform (2 × 150 bp paired-end reads).

Data analysis and batch effect correction

Single-cell RNA sequencing (scRNA-seq) data were analyzed as previously described.[48,49] Briefly, a filtered gene expression matrix for all 18 samples was generated using kallisto/bustools (kb v0.24.4) and concatenated using anndata (ad v0.7.6).[49] Cells and genes were filtered using the sc.pp.filter_cells and sc.pp.filter_genes functions from the Scanpy (sc v1.11.1) package for further analysis. To minimize technical artifacts from low-quality cells and potential doublets, cells meeting the following criteria were excluded: (1) fewer than 500 or more than 20,000 unique molecular identifiers (UMIs); (2) fewer than 100 or more than 5,000 detected genes; or (3) more than 10% of UMIs derived from mitochondrial genes, more than 50% of UMIs derived from ribosomal genes, or more than 5% of UMIs derived from hemoglobin genes. Second, genes that were expressed in at least three cells were selected for downstream analysis.

Potential doublets were identified using the Scanpy external module Scrublet[50] via the sc.external.pp.scrublet function with default parameters, designating cells with a doublet score >0.25 as predicted doublets. Raw UMI counts were normalized to a library size of 10,000 reads per cell using sc.pp.normalize_total to enable direct comparison across cells, followed by natural log-transformation (sc.pp.log1p). The log-transformed expression matrix was used for all downstream analyses. Highly variable genes (HVGs) were identified using sc.pp.highly_variable_genes, selecting a consensus set of the top 2,000 genes exhibiting the greatest cell-to-cell variability. Ribosomal and mitochondrial genes were excluded from the HVG list as previously described.[51] The HVG-restricted expression matrix was then used for downstream data integration. Each gene was subsequently scaled to unit variance and zero mean, with values exceeding 10 clipped to the maximum.

Datasets were integrated by computing principal component analysis (PCA) followed by batch-effect correction with Harmony. PCA was performed using sc.tl.pca with svd_solver = "arpack", and the top 50 principal components were retained. Harmony integration was then applied via Scanpy's external.pp.harmony_integrate function,[52] with sample and dataset variables as covariates (theta = 2.5 and 1.5, respectively). Nearest neighbor graph of cells was built using the sc.pp.neighbors function with batch-corrected matrix.

Cell clustering and annotations

Cells were clustered using the Louvain algorithm (sc.tl.louvain function) in two rounds. An initial round (resolution = 2.0) identified nine major cell types according to canonical marker genes (CellMarker 2.0 database)[31,53] (Figure S2 and Table S2): B cells, plasma cells, $CD4^+$ T cells, $CD8^+$ T cells, γδ T cells, mucosal-associated invariant T (MAIT) cells, natural killer (NK) cells, monocytes, and DCs. In the second round, Louvain clustering (resolution 1.0–1.5) was applied separately within $CD4^+$/$CD8^+$ T cells, B cells, NK cells, monocytes, and DCs to resolve subclusters. Subclusters were manually annotated based on canonical marker genes[31,53] and further validated using DEGs computed with the sc.tl.rank_genes_groups function.

Cell trajectories were inferred using partition-based graph abstraction (PAGA) implemented in Scanpy (v1.11.1),[54] revealing continuous transitions across cell states. Differentially expressed genes (DEGs) were identified with sc.tl.rank_genes_groups ("Wilcoxon rank-sum test" and "use_raw = True"), comparing cluster membership or vaccination condition, and filtered by Benjamini–Hochberg–adjusted $p < 0.05$ and absolute log fold-change >0.5. Ligand–receptor interactions were profiled using CellPhoneDB (https://github.com/ventolab/CellphoneDB).[55] Significant interactions were identified based on the tool's permutation testing framework, using the recommended p-value threshold of <0.05.

Identifying changes in immune cell proportion

The relative abundances of immune cell types and subtypes were compared across vaccination conditions using the Kruskal–Wallis test. For each cell population, three pairwise post-hoc comparisons (FJ vs. NJ, SJ vs. NJ, and SJ vs. FJ) were conducted, with Bonferroni correction applied to control the family-wise error rate. Vaccine dose-specific enrichment of cell populations was quantified as the ratio of observed to expected cell counts ($R_{O/E}$), calculated as described.[48]

Determining cell state scores

Cell type–specific activation and functional states were quantified across vaccination groups using gene set scoring. Gene sets representing proinflammatory cytokines, inflammatory responses, T cell exhaustion, and cytotoxic activity were curated from published sources[26,31,56] (Table S3), and the type I interferon signaling pathway (GO:0060337) gene set was obtained from the Enrichr repository (GeneOntology.org). Scores were computed in Scanpy (sc.tl.score_genes) as the normalized mean expression of genes in each set. For each score, three pairwise post hoc comparisons (FJ vs. NJ, SJ vs. NJ, and SJ vs. FJ) were conducted, with Bonferroni correction applied to control the family-wise error rate.

QUANTIFICATION AND STATISTICAL ANALYSIS

Statistical analyses and data visualization were performed using Python and R. Statistical significance is indicated in all figures as follows: ns, not significant ($p > 0.05$); *$p \leq 0.05$; **$p \leq 0.01$; ***$p \leq 0.001$; ****$p \leq 0.0001$.